


# Nonlinear-Lamb-wave-based plastic damage detection assisted by topologically designed metamaterial filters

Ze Liu<sup>1,2</sup>, Shengbo Shan<sup>3</sup> and Li Cheng<sup>1,2,4</sup> 

Structural Health Monitoring  
2023, Vol. 22(3) 1828–1843  
© The Author(s) 2022  
Article reuse guidelines:  
sagepub.com/journals-permissions  
DOI: 10.1177/14759217221114525  
journals.sagepub.com/home/shm  


## Abstract

Owing to their high sensitivity to material microstructural defects, nonlinear guided waves (NGWs) show great promise for the early detection of incipient damages, conducive to numerous structural health monitoring (SHM) applications. In an SHM system, however, inevitable non-damage-related nonlinear sources exist, which may overwhelm the damage-induced nonlinear components and in turn jeopardize the practical efficacy of the detection methodology. Therefore, these deceptive nonlinear interferences need to be mitigated or eliminated as much as practically possible. By embracing the concept of metamaterials, a wave filtering device, referred to as a meta-filter (MF), is developed in this paper. The MF is constructed through mounting periodic stubs on the surface of the structure under inspection to condition the probing signals under the second harmonic Lamb-wave-based SHM paradigm. Through topological optimization, the MF enables ultra-wide stop bands to eliminate the second harmonic Lamb waves of the probing waves while preserving their strong fundamental wave components. The band structure and the underlying mechanism, alongside the MF-enabled wave properties, are numerically investigated. Upon tactically introducing deceptive nonlinear sources such as the nonlinear adhesive bonding layers in a piezoelectric transducer-activated SHM system, the performance of the MF is examined from the SHM perspective, which is finally validated experimentally using a metal specimen containing local plasticized incipient damage. Results demonstrate that the designed MF allows for flexible selection of the excitation frequency on one hand, and entails significant enhancement of the detection ability of the NGW-based SHM system on the other hand owing to the customized band features arising from the topological optimization.

## Keywords

Structural health monitoring, nonlinear guided wave, second harmonic, elastic metamaterial, topology optimization, wave filter

## Introduction

Structural/material damages may jeopardize the operation and even the safety of engineering structures. They manifest in various forms and undergo different stages of development, ranging from the early stage of initiation (e.g., high-cycle fatigue<sup>1</sup> and creation of plastic zone alongside micro-structural changes<sup>2</sup>) to the more observable stage of physical defects (e.g., crack<sup>3,4</sup>) till the final stage of structural failure. To reduce such a risk, structural health monitoring (SHM) emerges as a potential solution to deliver online and real-time damage detection capabilities.<sup>5–8</sup> Among existing SHM approaches, the one based on ultrasonic guided waves has received wide attention due to its appealing advantages like low energy consumption, large inspection area, and high sensitivity to damages.<sup>5</sup> Relying on the

wave scattering features, conventional linear-guided-wave-based methods<sup>7,9</sup> offer a rather reliable way for

<sup>1</sup>Department of Mechanical Engineering, The Hong Kong Polytechnic University, Kowloon, Hong Kong

<sup>2</sup>The Hong Kong Polytechnic University Shenzhen Research Institute, Shenzhen, PR China

<sup>3</sup>School of Aerospace Engineering and Applied Mechanics, Tongji University, Shanghai, PR China

<sup>4</sup>The Hong Kong Branch of National Rail Transit Electrification and Automation Engineering Technology Research Center, The Hong Kong Polytechnic University, Kowloon, Hong Kong

### Corresponding author:

Li Cheng, Department of Mechanical Engineering, The Hong Kong Polytechnic University, 11 Yuk Choi Road, Hung Hom, Kowloon, 999077, Hong Kong.  
Email: li.cheng@polyu.edu.hk

the detection of macro-scale defects, typically in the millimeter range. However, linear approaches can hardly cope with the challenging problem of the early detection of small and incipient damages.

To tackle the problem, approaches based on nonlinear guided waves (NGWs) emerged as a promising alternative in recent years.<sup>10–16</sup> NGWs, resulting from the interaction between the primary waves with microstructural defects like dislocations,<sup>11,17</sup> micro-cracks,<sup>18</sup> and so forth, offer higher sensitivity to microstructural/material changes. Nonlinearities in structures may cause an energy shift from the primary excitation frequency of probing waves to other frequencies, exemplified by the second harmonic waves. As a result, the nonlinear guided wave–structural health monitoring (NGW-SHM) technique can potentially better cope with micro and incipient damages, thus attracting growing attention from the SHM community. Irrespective of the approaches used, the foremost request for the successful implementation of any NGW-SHM technique is to ensure the effective and accurate extraction of the damage-induced wave information. In practice, however, due to the use of higher harmonics and the incipient nature of the damage to be detected, damage-induced nonlinear wave components are usually weak, making their extraction extremely difficult.<sup>13</sup> Meanwhile, non-damage-related nonlinearities may also arise from various sources such as equipment, adhesive bonding layer, piezoelectric transducers (PZTs), and other undesired nonlinearities around the inspection area. Among all these possible nonlinearities, those at the actuating part have been shown to be dominant which severely interfere with the damage-related nonlinear signals, as demonstrated both experimentally and numerically in our previous works.<sup>13,19</sup> These deceptive factors may overwhelm the actual damage information and result in detection failure. Therefore, it is crucial to eliminate these deceptive nonlinear components in the probing waves before they arrive at the detection area. To highlight the damage-related wave components, the most commonly used approach consists in carefully tuning the transducer size and wave excitation frequency based on the frequency tuning curves.<sup>13,20</sup> An excitation frequency locating at the valley of the frequency tuning curve would ensure a reduced energy level of the wave mode at this specific frequency. However, such a method highly relies on a meticulous system modeling and tuning process. In addition, catered for one particular type of nonlinear component, the method requires a stringent selection of the transducer configuration and the excitation frequency, which is difficult to be generalized to other types of nonlinear sources and also makes the SHM system less flexible.

Metamaterials, as artificially architected composite structures/materials, have attracted considerable attention due to the boundless wave manipulation capability that they can offer.<sup>21,22</sup> Compared with natural materials, metamaterials enable extraordinary phenomena like negative refraction,<sup>23</sup> underwater acoustic shielding,<sup>24</sup> sound absorption<sup>25</sup> etc. More specific to elastic waves which are of major concern herein, elastic metamaterials have shown proven effectiveness to achieve energy isolation of guided waves.<sup>26</sup> Despite the extensive works on metamaterials, mainly in the context of physics and phenomenon discovery, their exploration for possible applications in SHM has been scarce. Bandgap effects<sup>27,28</sup> in a periodic lattice can prohibit wave propagation and offer possibilities for the manipulation of various nonlinear components in a system. For example, Tian et al.<sup>29</sup> proposed an aluminum-lead composite metamaterial to mitigate the undesired nonlinearity. The improved detection sensitivity for nonlinear sources induced by fatigue cracks was validated in a PZT-driven ultrasonic experiment. Sherwood et al.<sup>30</sup> installed periodically corrugated structures surrounding the PZT-actuator to filter out equipment-generated nonlinearity. The 3D-printed waveguide transducer alongside with metamaterial filter was experimentally tested to detect the second harmonics associated with a notch defect. By deploying a double-sided lead metamaterial filter on a plate, Shan et al.<sup>31</sup> improved the detection capacity of a generic NGW-SHM system for a microstructural change, created by a thermal-aging treatment in a nonlinear ultrasonic experiment.

While these previous attempts demonstrating the potential of the metamaterial-assisted NGW-SHM, the exploration of the idea is still at its embryonic stage of development and awaits further investigation from an SHM perspective. Due to the pre-defined basic topology of the metamaterial devices derived from the traditional empirical and intuitive design approaches, most existing works suffer from narrow bandgaps, which would directly limit the selection of the primary probing waves. This challenging issue calls for a systematic, tactic, and heuristic inverse-design paradigm to customize the bandgaps on demand. The idea was preliminarily investigated in our previous work,<sup>32</sup> with a focus on establishing a topology optimization framework for the general wave manipulation problems, with however no attempt on assessing the efficacy of the technique for concrete SHM applications. By comparison, the present study is specific to NGW-SHM, through addressing specific needs, problems, and phenomena pertinent to damage detection. More specifically, the design objective is set to accommodate NGW-SHM requirements in terms of dispersion properties of the metamaterial devices. Damage-wise, notch defects or

thermal damages have been examined in existing works.<sup>30,31</sup> However, detection of invisible incipient microstructural change induced by fatigue or plastic zones, which usually occur as a precursor of more visible structural damage in engineering structures, has not been considered in the context of metamaterial-assisted NGW-SHM. The above considerations motivate the present work.

More specifically, this paper proposes a tactically designed meta-filter (MF) with single-side and single-phase stubs, which is to be embedded into an NGW-SHM system to mitigate the undesired nonlinearity mainly from the actuation part of the structure under inspection. A unified inverse-design framework based on topology optimization is proposed to tailor-make the microstructure/topology of the MF to achieve controllable and wide bandgaps, which eventually would facilitate the implementation of the SHM strategy based on nonlinear Lamb waves. In particular, low-frequency Lamb wave mode pairs<sup>33–35</sup> are targeted in this work due to their slight dispersion. The inspection system with the embodiment of the designed MF is first examined through numerical simulations. Then, pitch-catch experimental tests are conducted to validate the improved diagnosis sensitivity of the MF-assisted NGW-SHM for incipient damage sources. The remaining part of this paper is organized as follows: Section “Topological design of meta-filter for deceptive nonlinearity mitigation” establishes the general methodology for the MF design, under specific NGW-SHM requirements. Then, Section “Numerical analyses” numerically examines the wave filtering performance of the designed MF in a PZT-driven NGW-SHM system. The efficacy of the proposed MF is then experimentally confirmed through artificially introducing plastic damage in a metallic beam in Section “Experimental validation.” Finally, Section “Conclusion” concludes the findings and contributions of this study.

### Topological design of meta-filter for deceptive nonlinearity mitigation

SHM technique based on the second harmonic waves is used as an example to illustrate the design approach. An MF, consisting of surface-mounted periodic stubs, is deployed on the structure to be inspected to eliminate the nonlinearity created in its actuation area, as shown in the typical PZT-driven SHM system in Figure 1(a). The designed MF is expected to simultaneously enable the passing of primary waves and the stopping of secondary waves. The former is to ensure sufficient wave energy to reach and interact with the damage to generate damage-induced second harmonic waves, whilst the latter is to avoid the interference to the damage-induced

second harmonic waves from the actuation. Upon deploying the designed MF, the received signal would not contain the non-damage-related nonlinear components and is thus purified, as illustrated by the sketch of signal evolution shown in Figure 1(d).

To achieve these wave manipulation functions, a unit cell, the minimum repeated element marked in Figure 1(a), is investigated, before getting the dispersion property of the entire MF using structural periodicity. The unit cell model shown in Figure 1(b) consists of the add-on stubs, the host plate, and a thin adhesive layer to bond the above two items. Through the design of the stub configuration, we can obtain the suitable MF satisfying the above NGW-SHM requirements. To this end, an inverse-design strategy based on topology optimization depicted in Figure 1(c) is adopted to tailor-make the stub in the design domain, which is discretized into a binary matrix ( $N \times N$  pixels) where “1” represents solid stub material while “0” the vacuum. Details of the topology optimization framework are introduced in the following section (Section “Topology optimization framework”).

### Topology optimization framework

Topology optimization is employed to engineer the dispersion relations of the MF<sup>32</sup> following the topological design procedure shown in Figure 1(c). The key issue is the definition of objective functions and the relevant constraints. Targeting at passing fundamental waves and stopping secondary waves, the functionality of the MF is extended to achieve maximum bandgap widths, allowing for a more flexible selection of the excitation frequency. This leads to the following objective functions, formulated in mathematic form as:

$$\text{Find: } \theta_n = 0 \text{ or } 1, \quad (1)$$

$$\begin{aligned} \text{Maximize: } F_t &= \max (2\Omega_{\text{pass}} \cap \Omega_{\text{stop}}) \\ &- \min (2\Omega_{\text{pass}} \cap \Omega_{\text{stop}}) \end{aligned} \quad (2)$$

$$\text{Subject to: } k = [0, \pi/a], \quad (3)$$

$$\min: d(\Sigma) \geq d_1. \quad (4)$$

where Equation (1) implies that in the binary coding, if the value of the  $n$ th pixel is set as “1”, the pixel would be filled with solid material while “0” for vacuum; In Equation (2),  $\Omega_{\text{pass}}$  and  $\Omega_{\text{stop}}$  represent the sets of pass bands and stop bands, respectively, and  $F_t$  denotes the objective function value, which is defined as the width of the intersection set of the stop bands and the double frequencies of the pass bands; In Equation (3), the wave number  $k$  is swept in the range of  $0-\pi/a$  ( $a$  is the periodic constant) to cover the  $\Gamma$ -X direction of the Brillouin zones; Equation (4) is a geometric constraint used to enhance the topology quality of the designed

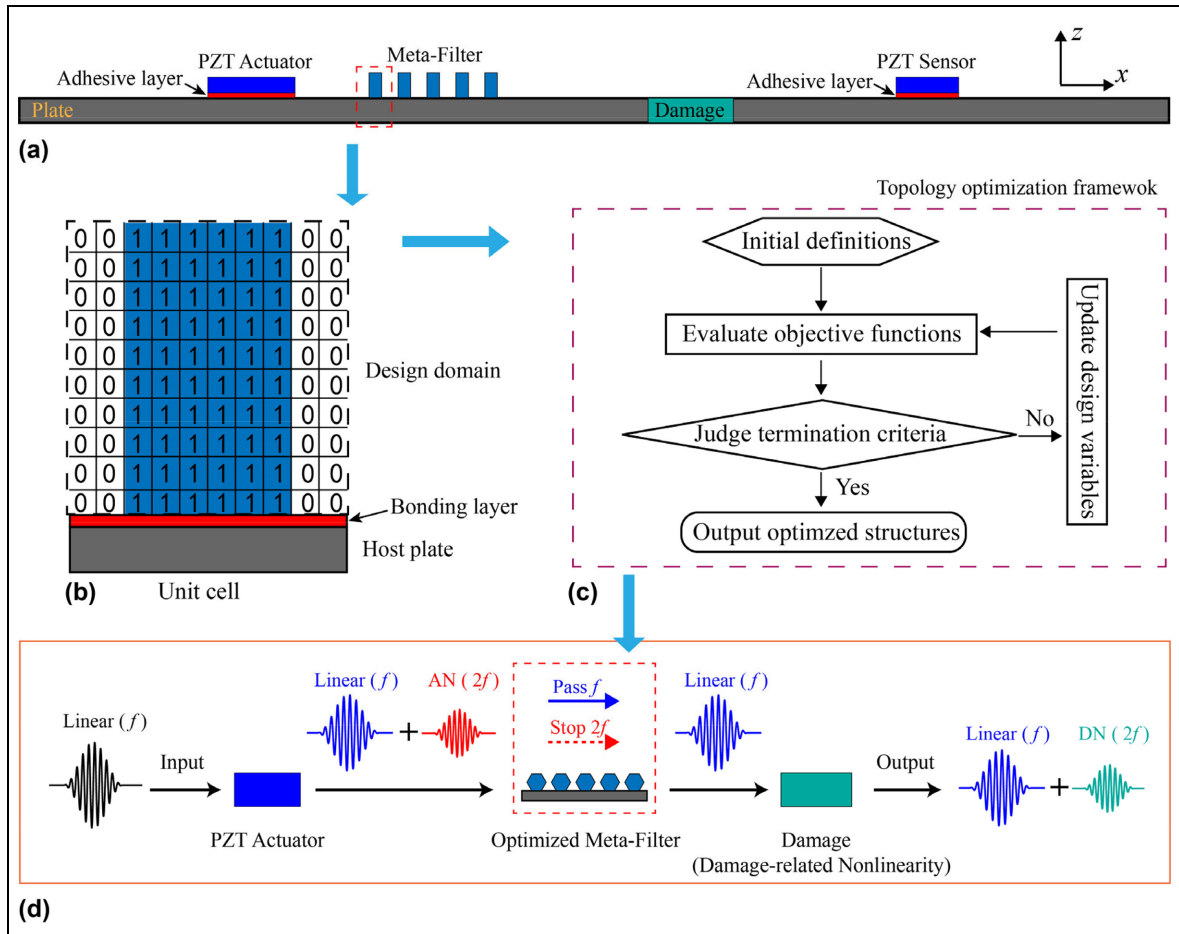


**Figure 1.** Schematic of the nonlinear-guided-wave-based structural health monitoring (SHM) system with topologically designed meta-filter. (a) A typical piezoelectric transducer (PZT)-driven SHM system with a meta-filter, (b) unit cell, (c) the topology optimization framework, and (d) evolution of signal components in the process, where adhesive nonlinearity (AN) is taken as a representative of non-damage-related nonlinearities, and DN denotes the damage-related nonlinearity.  $f$  represents the frequency of fundamental waves while  $2f$  for the frequency of the second harmonic waves.

structures. It indicates that the minimum geometric size of solid parts in the whole design domain should be larger than the prescribed parameter  $d_1$ , which is set as  $a/16$  herein.

To evaluate the above objective functions, COMSOL Multiphysics 5.2a is used to calculate the dispersion relations. Using the module of solid mechanics, 2D plane strain models are used for eigenfrequency study. Floquet periodic boundary conditions are applied to the left and right boundaries of the unit cell, with the other boundaries being set free. Wave number is swept in the range of  $0-\pi/a$  with a step of  $0.01 \times \pi/a$ . Mapped meshes are used for the domains of the host plate and the bonding layer, with 48 ( $N$  in design domain) layer meshes along the width direction ( $x$  direction) in both domains while, along the thickness direction ( $z$  direction), 10 layers for the host plate and 4 layers for the bonding layer are used. The design

domain adopts free triangular meshes with a maximum size of 0.15 mm (much smaller than wavelengths) as a good compromise between the computational time and the calculation accuracy.

Indeed, many optimization methods such as the solid isotropic material with penalization (SIMP) method,<sup>36,37</sup> genetic algorithm (GA),<sup>38,39</sup> and the level-set-based method<sup>40,41</sup> could be used for the topological design of metamaterials. In light of the complexity of the geometric constraints, image dealing operation, block number constraint, and simultaneous control of pass and stop bands in specific frequency regions in the present problem, we opted for GA, which is also widely used in the optimization community.<sup>22,42,43</sup> The method satisfies our needs with acceptable computational time using parallel technique. In principle, other optimization algorithms might be also feasible for this problem, including the SIMP-based method, which, as

**Table 1.** Geometric size and material parameters of the unit cell model.

	Material	Width (mm)	Height/thickness (mm)	Density $\rho$ (kg/m <sup>3</sup> )	Lame constants	
					$\lambda$ (GPa)	$\mu$ (GPa)
Host plate	Aluminum	6	2	2700	51.1	26.3
Bonding layer	Adhesive	6	0.05	1080	1.87	0.468
Design domain	Lead	6	6	11,600	42.0	14.9

a typical gradient-based topology optimization method, attracts vast attention due to its high efficiency.

The GA-based topology optimization procedure is performed as follows.<sup>39,43</sup> An initial population with  $M$  individuals is randomly generated. Then, finite element simulations are conducted to calculate the objective values of all individuals, according to Equations (1)–(4). Perform genetic operations including linear selection, uniform crossover with the possibility  $P_c$  and uniform mutation with the possibility  $P_m$ , to update the individuals. Before the next generation, abuttal entropy processing is conducted to improve the topology quality of the structures, and the total number of blocks within the design domain is restricted to one for

the sake of convenient implementation. Conduct the single-elitism strategy. If the termination criterion is not met, go to the next iteration and perform the same procedure as above; otherwise, end the procedure and output the final optimized structure by assembling all solid pixels.

### Optimized broadband meta-filter

Following the aforementioned inverse-design scheme, the unit cell is tailored to deliver broad stop bands in the second harmonic frequency range and simultaneously pass bands at the fundamental wave frequency region. For the low-frequency Lamb wave mode pairs, the bandgap range is preset at 100–200 kHz, corresponding to the excitation frequency of 50–100 kHz for pass bands. The geometric size and material properties of the unit cell model (Figure 1(b)), including the host plate, adhesive bonding layer, and the add-on components are defined in Table 1. Lead is used as the stub material, which exhibits very different material properties from those of the aluminum plate, thus creating distinct impedance mismatching between the two media, which is conducive to the generation of wide bandgaps. Indeed, the material selection is flexible and other types of stub materials can also be considered to implement the proposed idea. In the GA, the crossover and mutation proportions are 0.9 and 0.02, respectively. Each population contains 30 individuals. The design domain is first meshed into  $16 \times 16$  pixels and finally reaches the refined  $48 \times 48$  pixels. Besides, a prescribed symmetry is applied to the design domain so as to reduce the design variables by half. COMSOL Multiphysics 5.2a and MATLAB, on a Windows cluster with Intel Xeon Scalable Gold 6248R CPU @ 3.0 GHz and 48 cores, are used to perform the procedure. The whole optimization procedure runs for 1000 generations (500 for coarse pixels and the latter 500 for fine pixels), which totally cost around 26.3 h.

Starting from a randomly generated configuration, the final optimized stub of the MF is derived by gradually tailoring the microstructures, as shown by some representative intermediate topologies in Figure 2(a). The evolution curve manifests that the structures with good bandgap performance can be captured in the

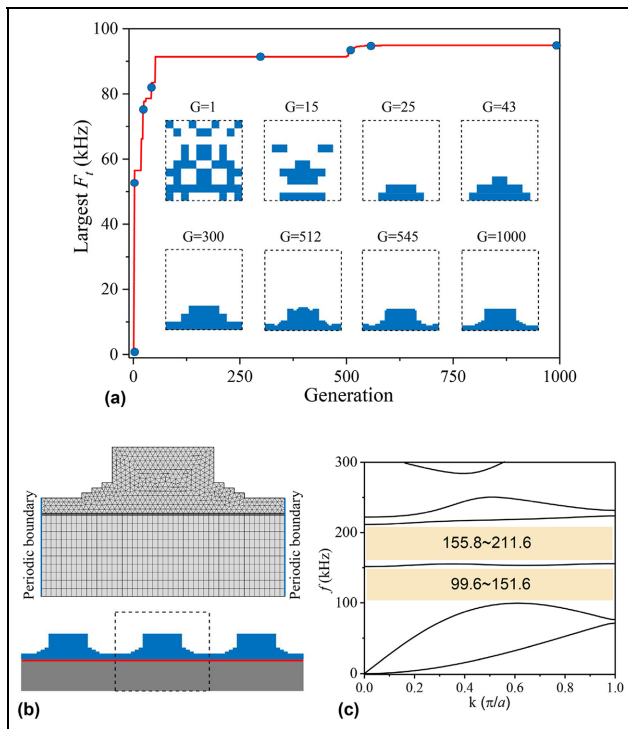


**Figure 2.** The optimization results: (a) the evolution history, (b) the optimized structure with a zoom-in finite element model of the unit cell, and (c) the corresponding dispersion relations. The bandgap regions are highlighted with shadows.

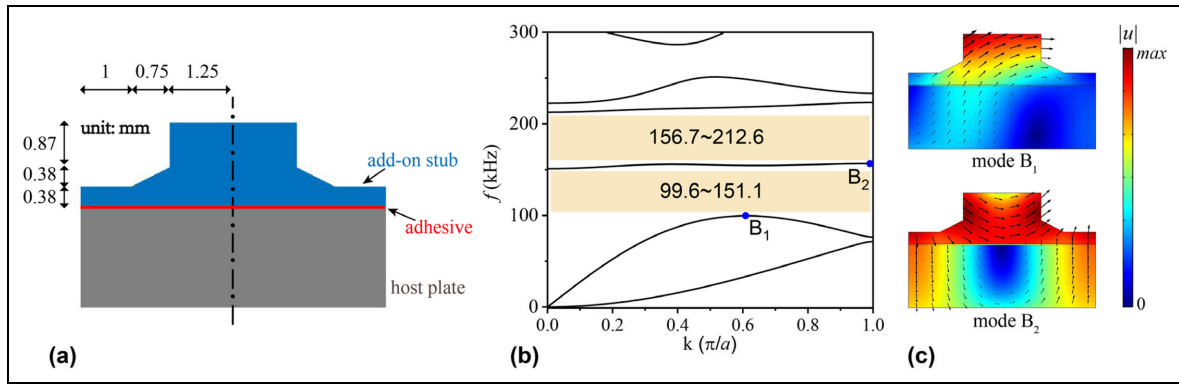


**Figure 3.** The simplified structure: (a) geometric parameters, (b) dispersion relations, and (c) two typical modes.

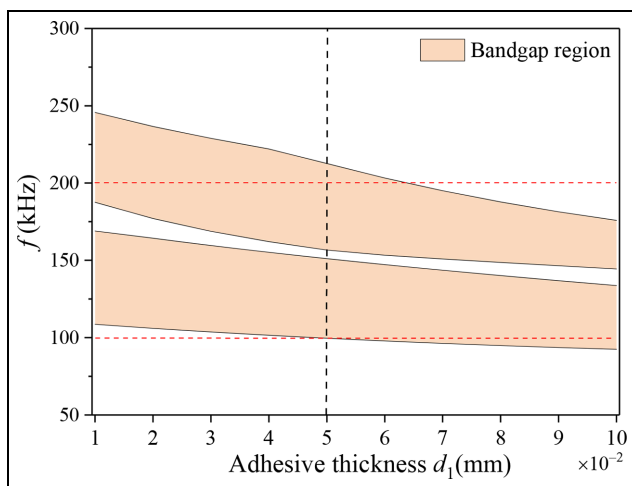


**Figure 4.** Bandgap ranges versus different thicknesses of adhesive layers.

early stage of iteration. The optimized structure alongside the finite element model and corresponding dispersion relations are depicted in Figure 2(b) and (c), respectively. It is relevant to note that ultra-wide bandgaps (95 kHz out of a 100 kHz range) are observed in the prescribed range. To facilitate fabrication, the edges of the stubs are smoothed to reach the simplified configuration in Figure 3(a). The dispersion curve comparison of the optimized structure and the simplified structure (Figures 2(c) and 3(b)) shows that the post-processing operation does not significantly affect the wide bandgaps obtained before. Topology-wise, the optimized MF is composed of relatively simple-shaped and interconnected stubs. In Figure 3(c), the lower-edge modes ( $B_1$  and  $B_2$ ) of the two bandgaps clearly exhibit scattering features, where the color and arrow denote the displacement value and the direction of the particle vibration. Since the wavelengths in the bandgap regions are in the same order of magnitudes with the periodic constant, it is concluded that the bandgaps

originate from the Bragg scattering effect. The strong contact between the add-on stubs and the host plate, as shown in Figure 3(a), enhances the coupling between the stub modes and the guided wave modes, which is conducive to the generation of wide bandgaps. In addition, rotational modes can be observed in the stub parts of modes  $B_1$  and  $B_2$ , especially for mode  $B_2$ . These modes contribute to the generation of flat bands, as evidenced by the third band (including mode  $B_2$ ) in Figure 3(b), allowing for the widening of the bandgaps.

Since the thickness of the bonding layer is hard to be precisely controlled in practical implementations of the MF, its effects on the achieved bandgaps are analyzed herein. Around the nominal value of 0.05 mm adopted before, the bonding thickness is varied from 0.01 to 0.10 mm. The results of bandgap positions versus bonding thicknesses are shown in Figure 4, which show that the bandgaps, albeit slightly affected, basically remain stable in terms of both range and width. Recalling the modes in Figure 3(c), it is observed that the displacement does not concentrate on the bonding area, which implies that changes of the bonding area would not greatly affect the modes and bandgaps. This property enhances the tolerance of the installation of the MF. In summary, the designed MF delivers broad bandgaps with NGW-SHM specific characteristics and robustness with relatively simple configuration comprising bottom-interconnected unit cells.

## Numerical analyses

Finite element simulations are conducted to assess the performance of the topologically designed MF. The transmission model in Figure 5 contains 10 unit cells that are attached on an 800 mm long and 2 mm thick plate. PZT-5H is used as actuator and sensor whose dimension is 30 mm  $\times$  0.3 mm and 8 mm  $\times$  0.3 mm, respectively. Their piezoelectric parameters are tabulated in Table 2. The bonding layers under both the

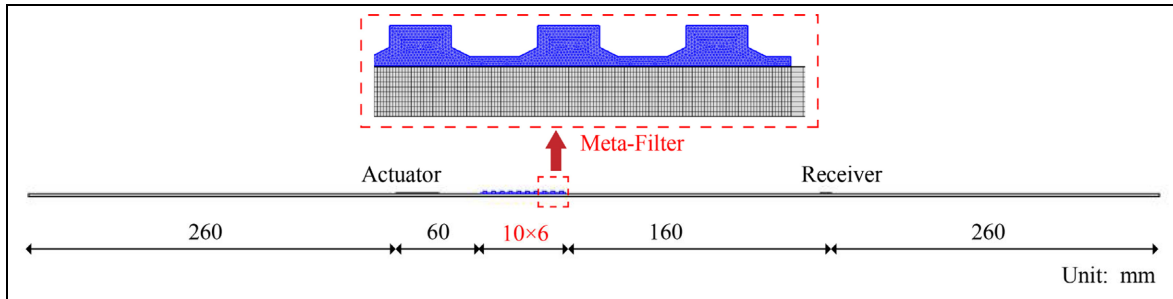


**Figure 5.** Simulation model.

**Table 2.** Material parameters of the PZT-5H.

$\rho$ (kg/m <sup>3</sup> )	$\lambda$ (GPa)	$\mu$ (GPa)	$d_{31}$ (pm/V)	$d_{33}$ (pm/V)	$\epsilon_{11}$	$\epsilon_{33}$
7650	41.7	23.5	-210	472	2270	2130

$d$  denotes the piezoelectric coefficient;  $\epsilon$  denotes the dielectric constant; the subscripts 1 and 3 represent  $x$  and  $z$  directions, respectively.

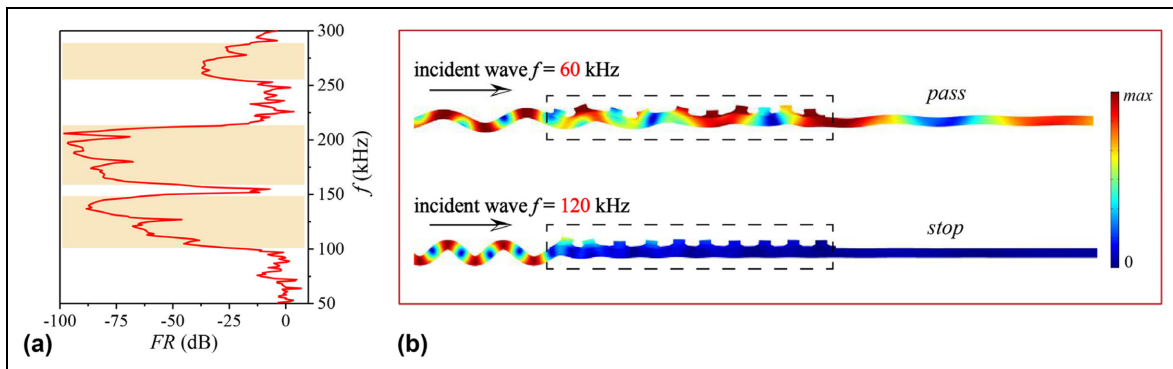


**Figure 6.** Numerically simulated wave transmission: (a) the frequency-domain responses and (b) the displacement fields at 60 kHz in the pass band and 120 kHz in the stop band.

PZTs and the add-on stubs are 0.05 mm thick. The model arrangement is depicted in Figure 5.

Using solid mechanics module of COMSOL, frequency analysis is used to calculate the frequency response of the 2D plane strain model. A prescribed displacement load along the  $z$  direction is applied on the actuation area. As shown in Figure 5, mapped meshes are used to discretize the host plate and the bonding layer while free triangular meshes are utilized in the add-on stubs, whose sizes are the same as those in the unit cell model. The remaining plate parts use a mesh size of 0.5 mm to save computational time while ensuring the accuracy. Low-reflecting boundary conditions are applied to the left- and right-hand boundaries of the model to minimize reflected waves. The scanning frequency range locates in 50–300 kHz, with a step size of 5 kHz. The frequency response function, defined as  $FR = 20 \log(u_1/u_0)$  with  $u_1$  and  $u_0$  being the

displacement amplitudes of the receivers with and without the MF respectively, is utilized to quantify the level of the wave attenuation. Using this index, the FR of the system with the designed MF is shown in Figure 6(a), where a negative FR value implies an attenuation of the wave within the corresponding frequency range. It can be found that the attenuation zones agree well with the previously predicted bandgap ranges (Figure 3(b)) marked with shadow, thus confirming the broadband filtering function of the MF. Moreover, the wave fields under the 60 kHz excitation (fundamental wave in the pass band) and the 120 kHz excitation (secondary wave in the stop band) are extracted and shown in Figure 6(b). It is explicit that the 60 kHz wave can pass the MF and continue to propagate along the plate while the 120 kHz wave component is prohibited.

As a first damaged scenario, material nonlinearity is introduced into the model. The adhesive nonlinearity

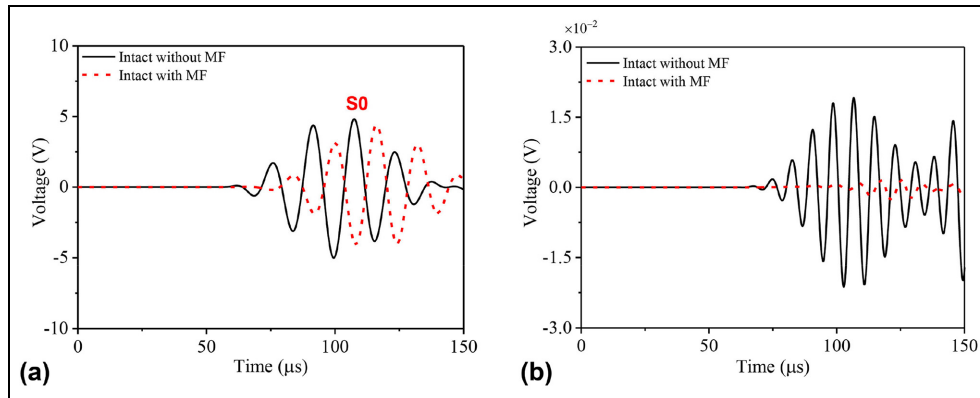


**Figure 7.** Numerically simulated temporal signals with and without the meta-filter (MF): (a) linear signals and (b) nonlinear signals induced by the adhesive nonlinearity.

under the PZT actuator is taken as a representative of the non-damage-related nonlinear sources while the nonlinearity of the aluminum plate is introduced to mimic a damage in the plate under inspection, which is referred to as the damage-related nonlinearity. It is surmised that if the adhesive nonlinearity can be eliminated by the MF, other non-damage-related sources can, in principle, also be filtered out. In this model, the Landau-Lifshitz model,<sup>13,44</sup> describing the stress-strain relationship is adopted to define the material nonlinearity, including both the adhesive nonlinearity and the damage-related nonlinearity. The third order elastic constants  $\bar{A}$ ,  $\bar{B}$ , and  $\bar{C}$  are used to generate the second harmonics (adhesive nonlinearity:  $\bar{A}_{ad} = -20.9$  GPa,  $\bar{B}_{ad} = -8.3$  GPa, and  $\bar{C}_{ad} = -6.1$  GPa; aluminum nonlinearity:  $\bar{A}_{al} = -702.4$  GPa,  $\bar{B}_{al} = -280.8$  GPa, and  $\bar{C}_{al} = -205.6$  GPa).<sup>19</sup> These physical parameters adopted herein are considered rather realistic, which were derived based on experimental tests.<sup>19</sup> A 2D model with dimensions identical to those in Figure 5 is established in ABAQUS with implicit dynamic analyses. The time step is set to be  $1e-7$ s. Tie constraints are applied to the interfaces in different parts to ensure displacement continuity. An electric potential load is applied to the PZT actuator. CPE4 (plane strain quadrilateral) elements are used for the host plate and the bonding layer while CPE3 (plane strain triangle) elements for the add-on stubs, whose mesh sizes are set to be equal to those used in the COMSOL model. CPE4E (plane strain piezoelectric quadrilateral) elements are used to model the PZT actuator and sensor. A UMAT subroutine is coded to introduce the material nonlinearity associated with the adhesive and the aluminum. To extract the second harmonic information, two signals with inversed phases are respectively actuated. Through the superposition of the two received signals, the primary waves would be eliminated and the remaining

parts are mainly the secondary waves,<sup>45</sup> referred to as the nonlinear components. On the other hand, since the intensity of the fundamental wave is much stronger than that of the generated secondary wave, the received original signal mainly contains the fundamental wave, referred to as the linear components.

With only the adhesive nonlinearities under the PZT actuator and the add-on stubs in the system (without damage-related nonlinearity), the filtering function of the designed MF for the generated non-damage-related secondary waves is examined via time-domain analyses. Under a 5-cycle and 160 V-peak tone burst excitation at a central frequency of 60 kHz, the linear and nonlinear temporal signals of the S0 mode waves are given in Figure 7(a) and (b), respectively. The MF does not seem to significantly alter the amplitude of the linear signal; the nonlinear signal originating from the adhesive nonlinearity is drastically reduced due to the band-gap effect, in agreement with the design target. At the same time, a phase lag of the linear signals, originating from different wave velocities with/without the MF, is observed in Figure 7(a). This, however, is not a problem for the present detection method based on higher harmonics. The method is based on signal intensity, rather than the signal phase, to characterize/identify damage.

The excitation then scans the frequency range of 50–100 kHz (corresponding to the estimated bandgap range), with other input parameters being identical to the above 60 kHz case. The discretized excitation frequencies are [55, 60, 70, 80, 90, 95] kHz. To quantify the attenuation effect of the designed MF in time domain, a transmission factor (TF) is defined as follows:

$$TF = \frac{CA_{\text{meta-filter}}}{CA_{\text{pristine}}} \quad (5)$$



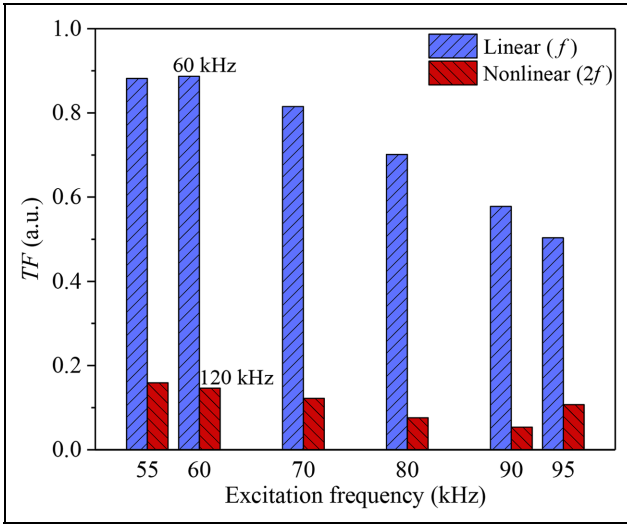


**Figure 8.** Transmission performance of the linear and nonlinear components under excitation frequencies of [55, 60, 70, 80, 90, 95] kHz.

$$CA = \sqrt{\sum_{t=t_0}^{t_1} [A(t)]^2} \quad (6)$$

where TF denotes the ratio of the characteristic amplitudes (CAs) with ( $CA_{\text{meta-filter}}$ ) or without ( $CA_{\text{pristine}}$ ) the MF; CA is the sum of the considered temporal signal, used to represent the energy level;  $A(t)$  denotes the voltage value at the time point  $t$ , ranging from  $t_0$  to  $t_1$ .

The linear and nonlinear wave transmissions are shown in Figure 8, for the first 0.3 ms temporal signals ( $t_0 = 0$  and  $t_1 = 0.3$  ms). It is evident that, compared with the relatively large TFs of the linear signals, the

nonlinear TFs are very small. For example, in the 60 kHz case, the linear TF is 0.89 while the nonlinear one is 0.15. This indicates that most fundamental wave energy can be transmitted while that of the secondary wave induced by the adhesive nonlinearity is drastically reduced. This phenomenon is widely observed in all bandgap frequencies, which manifests the broadband and customized filtering functions of the designed MF.

To further demonstrate the enhanced damage diagnosis capability of the MF-assisted NGW-SHM system, damage-related nonlinearity is introduced while the adhesive nonlinearity is removed. A 30 mm × 2 mm region on the aluminum plate between the MF and PZT sensor is defined as nonlinear material, which is used to represent the damage source. For the same 60 kHz case, Figure 9(a) shows that the damage-related signal changes still hold sufficiently high intensity, albeit a slight decrease caused by the MF. Moreover, Figure 9(b) shows the nonlinear intensity of the cases without and with the MF, respectively. In each case, the intensity of the adhesive nonlinearity, quantified by the index CA defined in Equation (6), is taken as the baseline to normalize the intensity of the damage-induced nonlinearity. In the pristine system, the intensity of the adhesive nonlinearity is larger than that of the damage-related nonlinearity, suggesting that the identified nonlinearity is mostly not attributed to actual damage. After introducing the MF, the intensity of the adhesive nonlinearity is greatly reduced and consequently becomes much lower than that of the damage-related nonlinearity, which implies that the acquired nonlinear information is genuinely originated from the material damage. Therefore, the damage detection capability of the NGW-SHM is enhanced with the aid of the designed MF.

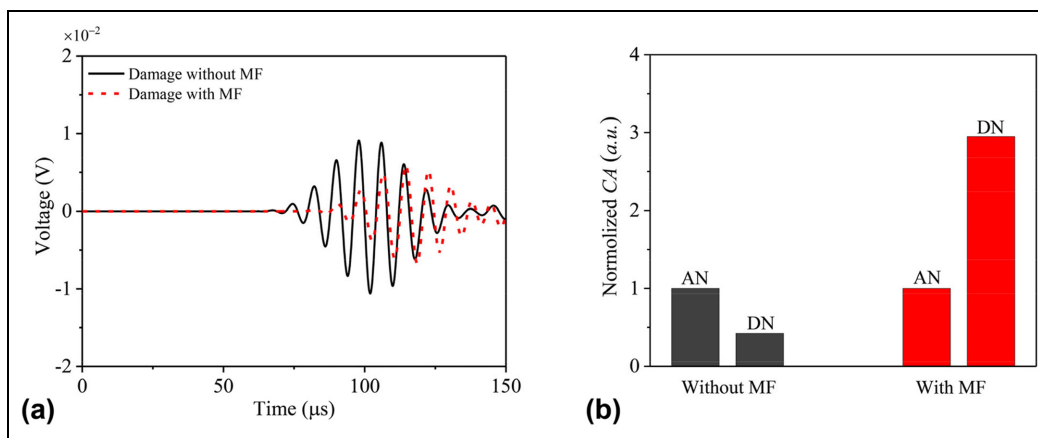


**Figure 9.** (a) Nonlinear signals induced by the damage-related nonlinearity (DN) and (b) intensity comparison of the adhesive nonlinearity (AN) and DN respectively with or without the MF. In each case, the intensity of the AN, quantified by the index characteristic amplitudes (CAs) defined in Equation (6), is taken as the baseline to normalize the intensity of the DN.

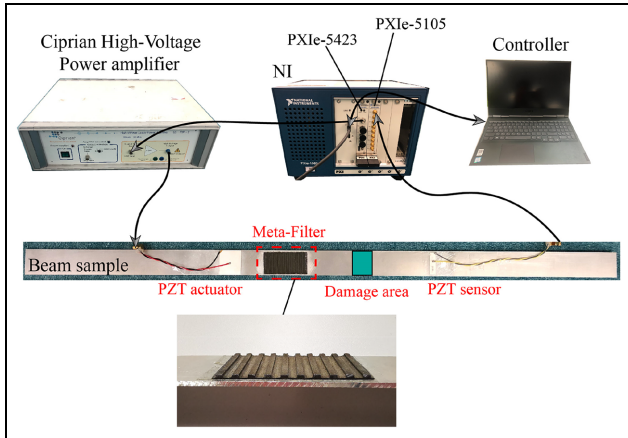


**Figure 10.** Experimental set-up.

## Experimental validation

Experiments are conducted to assess the performance of the designed MF in a PZT-driven system. An MF sample with 10 unit cells is fabricated through mechanical cutting with a manufacturing accuracy of 0.1 mm. The size of the aluminum (2024-T3) beam is 800 mm  $\times$  30 mm  $\times$  2 mm. PZT patches with dimensions of 30 mm  $\times$  30 mm  $\times$  0.3 mm and 8 mm  $\times$  30 mm  $\times$  0.3 mm, respectively, are used as the actuator and sensor. The locations of the PZTs and MF are the same as those used in simulations shown in Figure 5. The epoxy glue “UHU PLUS ENDFEST 300” is used to attach the PZTs and the MF to the beam. The experimental set-up used to test an aluminum beam sample is

shown in Figure 10, which mainly consists of a computer controller, National Instrument (NI) with PXIe-5423 signal generation module and PXIe-5105 data acquisition module and Ciprian high-voltage power amplifier. The experiment procedure is as follows: 5-cycle tone burst excitation signals with inversed phases are first defined in the controller and generated by the NI PXIe 5423 module. The signals are then amplified by the Ciprian power amplifier with the amplitude of 160 V, and feed the PZT actuator to generate Lamb waves, which propagate along the plate and are captured by the PZT sensor. Finally, the NI PXIe 5105 module records the received signal and sends the data to the controller. The scanned frequency ranges between 40 and 300 kHz, with a step size of 5 kHz. At each frequency, signals are repeated 100 times and then averaged to reduce environmental noise.

The pristine beam sample is first tested to provide a baseline. Then, the designed MF is installed and the corresponding signal is acquired. The temporal signals corresponding to the central frequency of 60 kHz (in the pass band) and 120 kHz (in the stop band) excitations are first extracted. It is evident that the former (Figure 11(a)) passes through the MF, albeit some alterations, while the latter (Figure 11(b)) is filtered out. The TFs (Equations (5) and (6)) within the entire 40–300 kHz range are then measured and shown in Figure 11(c). It follows that the wave attenuation phenomenon can be clearly seen from the small TF values within broad bandgap regions.

Note that non-damage-related nonlinear sources are implicitly and inevitably included in the above system.

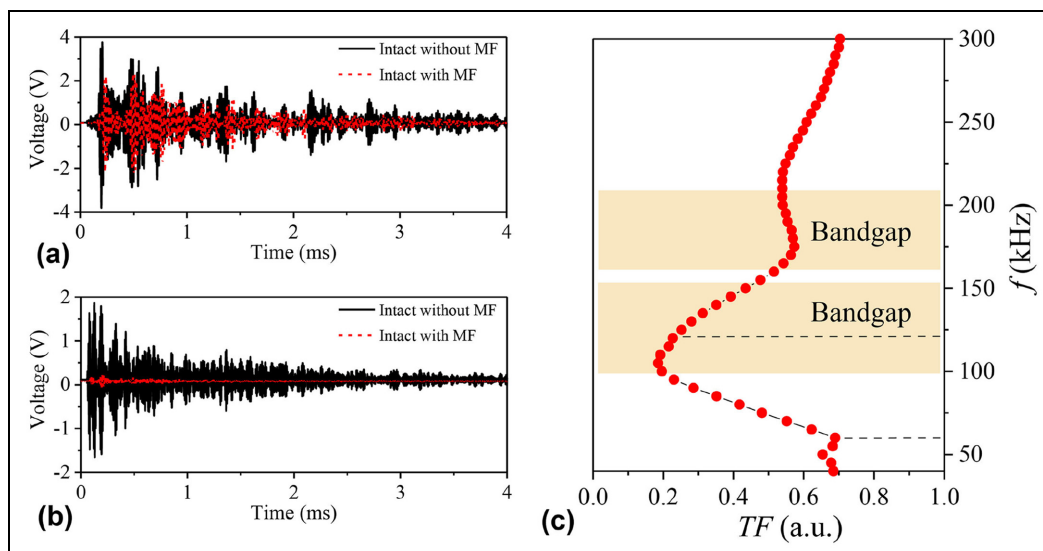


**Figure 11.** Experimentally measured wave transmissions with and without the meta-filter (MF), respectively: (a) temporal signals under 60 kHz tone burst excitation in the pass band, (b) temporal signals under 120 kHz tone burst excitation in the stop band, and (c) the transmission factor (TF).

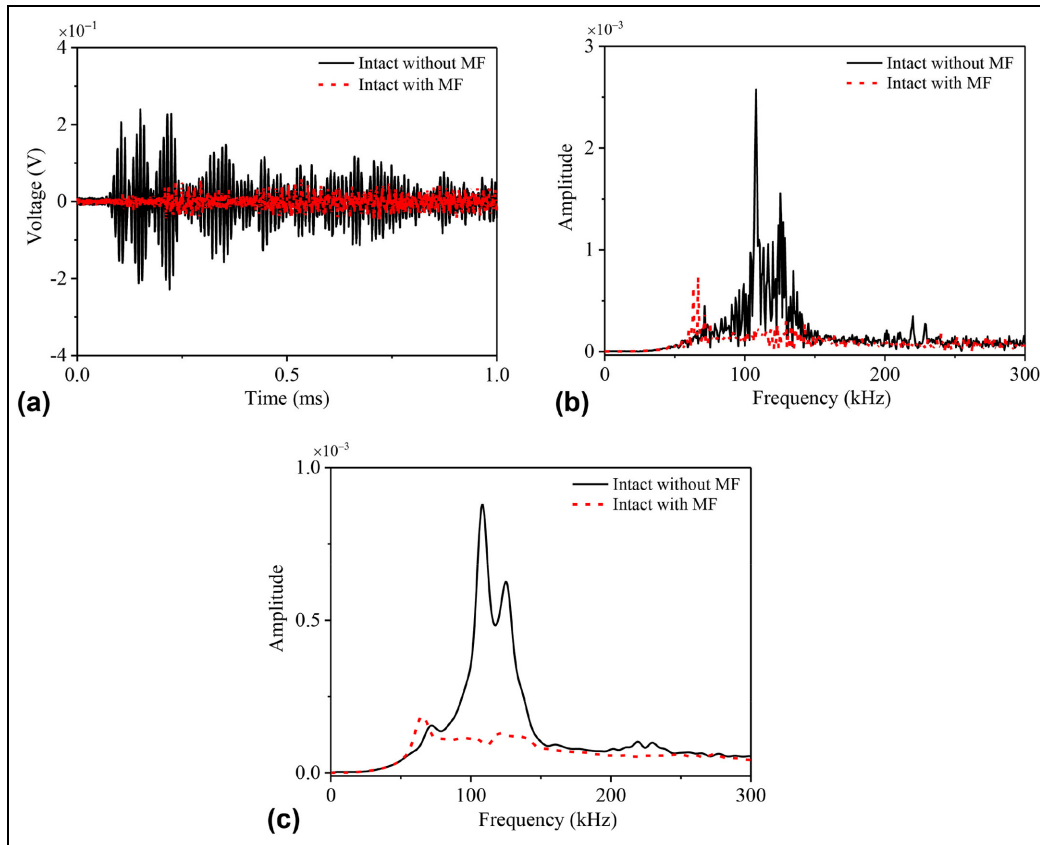


**Figure 12.** Non-damage-related nonlinearity under 60 kHz excitation, with and without the meta-filter (MF) in experiments: (a) the temporal signals, (b) the original frequency spectra, and (c) the smoothed frequency spectra.

As mentioned above, the extraction of the second harmonic waves is based on the superposition method,<sup>19,45</sup> which requires the two excitation signals to have perfectly opposite phases but identical amplitude. Through the superposition of the response signals with inversed phases, the fundamental waves can, in principle, be eliminated and the remaining parts are mainly the second harmonic signals. However, because of the experimental uncertainties like noise, the excitation signals might be not ideal in terms of amplitude and phase. This makes the two excitation signals not have precisely opposite phases and equal amplitude. As a result, the fundamental waves may not be completely eliminated in the superposed signals. Therefore, to focus on the second harmonic frequency region of interest, a Butterworth high-passing filter (above 80 kHz) is applied to the superposed signals to mitigate the fundamental wave components. Performing the above procedure, the processed temporal signals are shown in Figure 12(a). Meanwhile, corresponding spectra (Figure 12(b)) are also calculated via the Fast Fourier Transform. It is worth noting that the material damage has not been introduced in this system yet.

Therefore, the measured second harmonic components are regarded as the outcome of the non-damage-related sources. To compare the cases with and without the MF, a “smooth” operation (in MATLAB) is applied to the original frequency spectra. The smoothed spectra shown in Figure 12(c) manifest the distinct amplitude difference within the second harmonic region around 120 kHz of interest. It should be pointed out that this processing would not affect the evaluation of the amplitude difference between the two signals, and the wave filtering efficacy of the MF is still clearly seen. It can be concluded that, with the aid of the MF, the amplitudes of the deceptive nonlinear waves are drastically reduced in both temporal signals and corresponding frequency spectra.

Herein, a bending operation is conducted to create a plastic damage zone in the above beam sample to further examine the capability of the designed MF-assisted detection system. It has been demonstrated that the induced density dislocation arising from such operation is responsible for the generation of nonlinearity.<sup>11,17</sup> To mimic the damage accumulation process, four bending cycles are conducted step by step. More specifically,

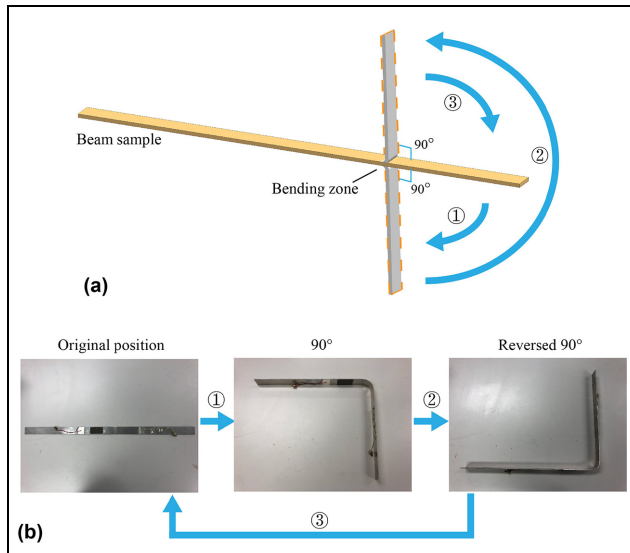


**Figure 13.** Bending operation to create a plastic damage zone in the beam sample: (a) schematic of one complete bending cycle and (b) the sample after one complete bending cycle used in the experiment.

one complete bending cycle is defined as follows: ① starting from the original position, the beam sample is first bent to  $90^\circ$  (clockwise or anticlockwise); ② then, bend  $180^\circ$  toward the opposite direction; ③ finally, resume to the original position by bending  $90^\circ$  back. The entire process and the final plasticized sample are shown in Figure 13.

Keeping the MF in place, one-cycle bending is first applied and examined. The measured linear signals (Figure 14(a)) show almost no difference compared to those from the original intact case, while the nonlinear signals (Figure 14(b)) change drastically. The results manifest that the energy of the measured nonlinear signals can be significantly enhanced as a result of the

bending operation on one hand, and the captured nonlinear signals are able to signal the occurrence of the incipient plastic zone on the other hand. With increasing bending cycles, the corresponding frequency spectra of the processed nonlinear signals under different cycles are shown in Figure 15(a). It is seen that the nonlinear signal amplitudes vary with the bending cycles associated with different stages of damages. To exhibit this evolution process clearly, the  $n$ -cycle ( $n$ -cycle denotes  $n$  bending cycles) damaged CAs of the nonlinear waves are calculated through benchmarking with the intact case. The normalized CAs in Figure 15(b) show the following variation trend: the nonlinear signal intensity first dramatically goes up, then gradually decreases before finally reaching a rather stable level. Similar phenomena in terms of nonlinearity evolution are also observed in another independent experiment reported in the literature.<sup>46</sup> In that study involving a similar bending treatment on a metal sample, the amplitudes of nonlinearities were also shown to decrease with the bending cycles after an initial increase. This, to some extent, provides an additional confirmation on the non-monotonic change of the nonlinear amplitudes presented in our work. Indeed, these phenomena can be explained from the perspective of micro-structural changes inside the material. It is widely admitted that the generation of material nonlinearity can be attributed to the dislocation density effect induced by plastic deformation. As reported in the literature,<sup>47,48</sup> there are two stages in the dislocation structure evolution of materials during plastic deformation: (a) the dislocation densities increase with plastic deformation; and (b) a dislocation rearrangement inside the material cells occurs and, as a result, the dislocation density would decrease or saturate. The above process is consistent with the evolution trend observed from the captured nonlinear amplitudes shown in this work.

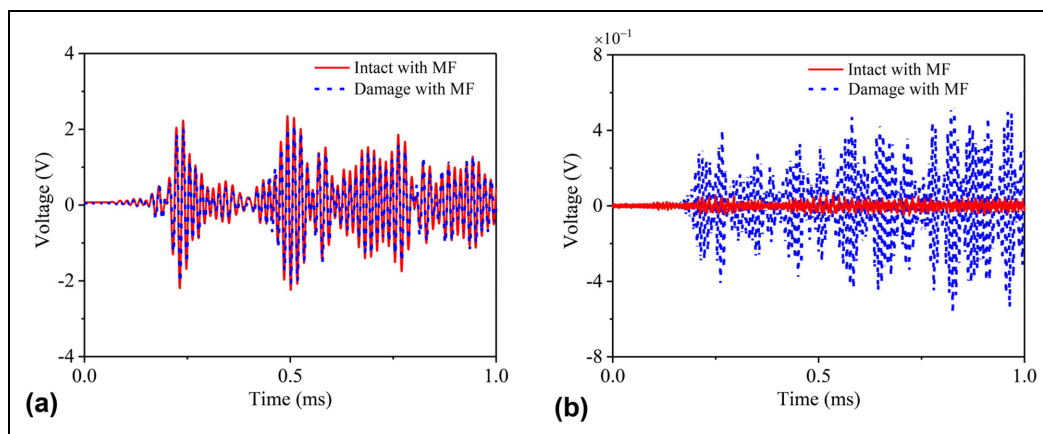


**Figure 14.** Temporal signals under 60 kHz excitation before and after introducing plastic damages in experiments, with the presence of the meta-filter (MF): (a) linear signals and (b) nonlinear signals.

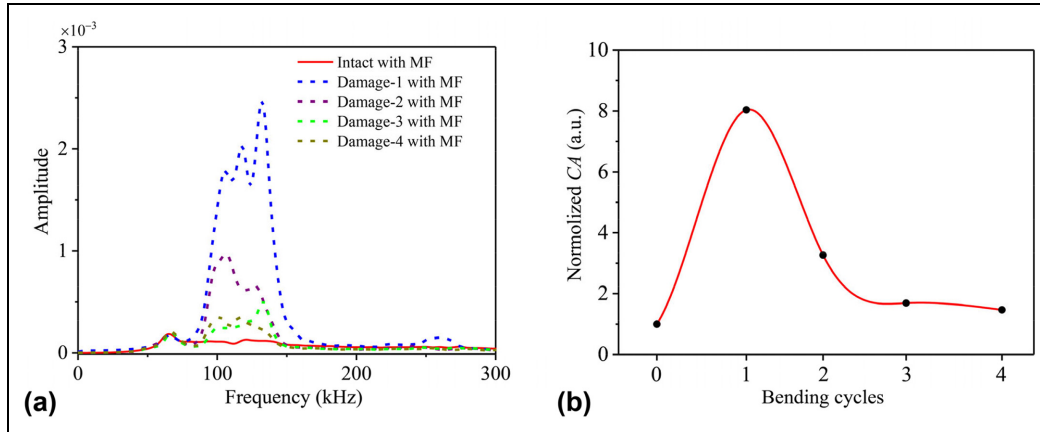


**Figure 15.** The damage-related nonlinearities at different stages under 60 kHz excitation with the presence of the meta-filter (MF) in experiments. Damage- $n$  denotes the case with  $n$  bending cycles. (a) Frequency spectra of the nonlinear signals under different bending cycles and (b) the variation trend of the normalized characteristic amplitudes (CAs) (benchmarked with the intact case) with respect to increasing bending cycles.

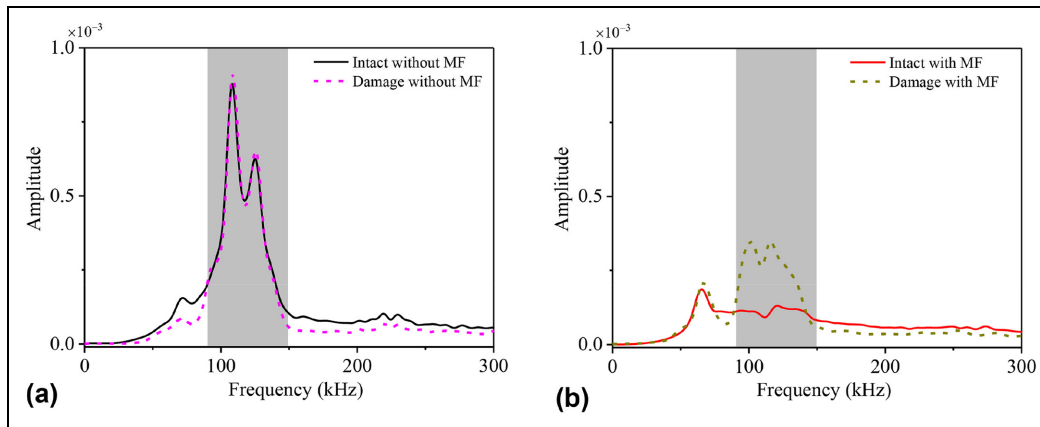


**Figure 16.** Comparisons of the damage-related nonlinear signal intensity captured on the damaged sample before and after removing the meta-filter (MF) in experiments: (a) without the MF and (b) with the MF. The shadow areas approximately indicate the second harmonic regions.

In the intact case with the MF in Figure 15(a), since the nonlinearities at the actuation area have been filtered out, the captured nonlinear signals can be attributed to the distributed nonlinearity (material nonlinearity of the plate for example) along the wave propagation path. It is observed that the non-damage-related distributed nonlinearity is rather weak in the present case as compared with that caused by the plastic damage, as evidenced by Figure 15(a). This is because the second harmonic wave energy accumulation arising from distributed nonlinearity relies on the so-called synchronism condition (the same phase velocity of the mode pair: the fundamental and second harmonic waves) while the excitation frequency used in our study does not rigorously satisfy this condition.

Finally, the MF is removed from the damaged beam for comparison with the cases with the MF. The

frequency spectra of the nonlinear waves of both cases are compared in Figure 16(a) and (b), in which the second harmonic regions around 120 kHz (90–150 kHz) are highlighted in shadow. It can be observed that without the MF (Figure 16(a)), the amplitudes of the nonlinear waves in the intact and the damaged cases are very similar, which confirm that the damage cannot be discerned without the MF, as opposed to Figure 16(b) where the MF is deployed. Through this comparison, the efficacy of the MF is validated from the damage detection perspective.

## Conclusions

In this study, the concept of metamaterial filters, referred to as MFs, is introduced and implemented into a NGW-based SHM system to mitigate the non-

damage-related nonlinear sources, so as to improve the detection capability for incipient damages. Originating from this SHM-specific demand and based on topology optimization, a unified inverse-design scheme is established to tailor-make MFs. In the context of nonlinear-Lamb-wave-based SHM, the MF is designed through tailoring the dispersion relations to ensure the passing of fundamental waves to reach and interact with damages to generate damage-induced second harmonic waves, whilst prohibiting the propagation of the second harmonic waves from the actuation area to avoid their interference to the damage-induced second harmonic waves.

Numerical simulations demonstrate the broadband wave filtering functionality of the designed MF with 10 unit cells, in the frequency regions well correlated with the bandgap regions predicted by dispersion analyses. Through tactically separating the non-damage-related and damage-related nonlinearities, the MF is shown to be able to effectively filter out the non-damage-related nonlinearities while retaining the damage-related nonlinearity information in the captured second harmonic Lamb wave signals. As a result, the damage-related nonlinear components dominate the received nonlinear signals, making the damage detection possible. Numerically predicted MF efficacy is also experimentally confirmed. The structural damage used in experiments is created through a well-controlled bending operation on a metallic beam sample. Bending cycles are varied to mimic the evolution of plasticized damages induced by the density dislocation effect. With the embodiment of the MF in the system, damage detection results show non-monotonous variation of the captured nonlinear energy level with the bending cycle, consistent with the observations reported in existing literature.

This work offers a novel approach to customize the high-performance SHM-specific MF to enhance the capability of NGW-SHM for incipient damage diagnosis. In a broader sense, the proposed method may also inspire the design and exploration of other innovative wave manipulation devices, specific to a given NGW-SHM requirement. Although this study focuses on the nonlinearities at the actuation area, the proposed MF can be tactically installed over the structure under inspection. In principle, as long as the strength of the incoming probing waves is strong enough, MFs can be installed either away, or close to the inspection area. Meanwhile, we recognize the need for considering other options to deal with other strong, localized yet non-damage-related nonlinearities near the damage area. This definitely deserves further research effort.


## Declaration of conflicting interests

The author(s) declared no potential conflicts of interest with respect to the research, authorship, and/or publication of this article.

## Funding

The author(s) disclosed receipt of the following financial support for the research, authorship, and/or publication of this article: This work was supported by the Research Grants Council of Hong Kong Special Administrative Region [PolyU 152013/21E]; the National Natural Science Foundations of China through SHENG project [Polish-Chinese Funding Initiative, 51961135302]; Research Fund of State Key Laboratory of Mechanics and Control of Mechanical Structures [Nanjing University of Aeronautics and Astronautics, China, Grant No. MCMS-E-0520K01]; the National Science Foundation of Shanghai [22ZR1462700]; the Fundamental Research Funds for the Central Universities; and the Innovation and Technology Commission of the HKSAR Government to the Hong Kong Branch of National Rail Transit Electrification and Automation Engineering Technology Research Center.

## ORCID iD

Li Cheng  <https://orcid.org/0000-0001-6110-8099>

## References

1. Hong M, Su Z, Wang Q, et al. Modeling nonlinearities of ultrasonic waves for fatigue damage characterization: theory, simulation, and experimental validation. *Ultrasonics* 2014; 54(3): 770–778.
2. Pruell C, Kim JY, Qu J, et al. Evaluation of plasticity driven material damage using Lamb waves. *Appl Phys Lett* 2007; 91(23): 231911–231911-3.
3. Masserey B and Fromme P. Fatigue crack growth monitoring using high-frequency guided waves. *Struct Health Monit* 2013; 12(5–6): 484–493.
4. Guan R, Lu Y, Wang K, et al. Fatigue crack detection in pipes with multiple mode nonlinear guided waves. *Struct Health Monit* 2019; 18(1): 180–192.
5. Giurgiutiu V. *Structural health monitoring: with piezoelectric wafer active sensors*. Amsterdam: Elsevier, 2007.
6. Farrar CR and Worden K. An introduction to structural health monitoring. *Philos Trans R Soc A Math Phys Eng Sci* 2007; 365(1851): 303–315.
7. Roy S, Lonkar K, Janapati V, et al. A novel physics-based temperature compensation model for structural health monitoring using ultrasonic guided waves. *Struct Health Monit* 2014; 13(3): 321–342.
8. Wang CH, Rose JT and Chang FK. A synthetic time-reversal imaging method for structural health monitoring. *Smart Mater Struct* 2004; 13(2): 415.
9. Yu L and Tian Z. Lamb wave structural health monitoring using a hybrid PZT-laser vibrometer approach. *Struct Health Monit* 2013; 12(5–6): 469–483.

10. Deng M and Pei J. Assessment of accumulated fatigue damage in solid plates using nonlinear Lamb wave approach. *Appl Phys Lett* 2007; 90(12): 121902.
11. Cantrell JH. Nonlinear dislocation dynamics at ultrasonic frequencies. *J Appl Phys* 2009; 105(4): 043520.
12. Xiang Y, Deng M and Xuan FZ. Creep damage characterization using nonlinear ultrasonic guided wave method: a mesoscale model. *J Appl Phys* 2014; 115(4): 044914.
13. Shan S, Cheng L and Wen F. Design of nonlinear-Lamb-wave-based structural health monitoring systems with mitigated adhesive nonlinearity. *Smart Mater Struct* 2018; 27(10): 105006.
14. Wang R, Wu Q, Yu F, et al. Nonlinear ultrasonic detection for evaluating fatigue crack in metal plate. *Struct Health Monit* 2019; 18(3): 869–881.
15. Lissenden CJ. Nonlinear ultrasonic guided waves—principles for nondestructive evaluation. *J Appl Phys* 2021; 129(2): 021101.
16. Wen F, Shan S and Cheng L. Third harmonic shear horizontal waves for material degradation monitoring. *Struct Health Monit* 2021; 20(2): 475–483.
17. Cash WD and Cai W. Dislocation contribution to acoustic nonlinearity: the effect of orientation-dependent line energy. *J Appl Phys* 2011; 109(1): 014915.
18. Wen F, Shan S and Cheng L. Immunity of the second harmonic shear horizontal waves to adhesive nonlinearity for breathing crack detection. *Struct Health Monit*. Epub ahead of print 6 December 2021. DOI: 10.1177/14759217211057138.
19. Shan S, Cheng L and Li P. Adhesive nonlinearity in Lamb-wave-based structural health monitoring systems. *Smart Mater Struct* 2016; 26(2): 025019.
20. Shan S and Cheng L. Two-dimensional scattering features of the mixed second harmonic A0 mode Lamb waves for incipient damage localization. *Ultrasonics* 2022; 119: 106554.
21. Liu Z, Zhang X, Mao Y, et al. Locally resonant sonic materials. *Science* 2000; 289(5485): 1734–1736.
22. Dong HW, Shen C, Zhao SD, et al. Achromatic metasurfaces by dispersion customization for ultra-broadband acoustic beam engineering. *Natl Sci Rev*. Epub ahead of print 24 February 2022. DOI: 10.1093/nsr/nwac030.
23. Pendry JB. Negative refraction makes a perfect lens. *Phys Rev Lett* 2000; 85(18): 3966.
24. Dong HW, Zhao SD, Miao XB, et al. Customized broadband pentamode metamaterials by topology optimization. *J Mech Phys Solids* 2021; 152: 104407.
25. Mei J, Ma G, Yang M, et al. Dark acoustic metamaterials as super absorbers for low-frequency sound. *Nat Commun* 2012; 3(1): 1–7.
26. Badreddine Assouar M and Oudich M. Enlargement of a locally resonant sonic band gap by using double-sided stubbed phononic plates. *Appl Phys Lett* 2012; 100(12): 123506.
27. Hedayatrasa S, Abhary K, Uddin MS, et al. Optimal design of tunable phononic bandgap plates under equibiaxial stretch. *Smart Mater Struct* 2016; 25(5): 055025.
28. Liu Z, Qin KQ and Yu GL. Partially embedded gradient metabarrrier: broadband shielding from seismic Rayleigh waves at ultralow frequencies. *J Eng Mech* 2020; 146(5): 04020032.
29. Tian Y, Shen Y, Rao D, et al. Metamaterial improved nonlinear ultrasonics for fatigue damage detection. *Smart Mater Struct* 2019; 28(7): 075038.
30. Sherwood GR, Chronopoulos D, Marini A, et al. 3D-printed phononic crystal waveguide transducers for nonlinear ultrasonic damage detection. *NDT&E Int* 2021; 121: 102456.
31. Shan S, Wen F and Cheng L. Purified nonlinear guided waves through a metamaterial filter for inspection of material microstructural changes. *Smart Mater Struct* 2021; 30(9): 095017.
32. Liu Z, Shan S, Dong HW, et al. Topologically customized and surface-mounted meta-devices for Lamb wave manipulation. *Smart Mater Struct* 2022; 31(6): 065001.
33. Wan X, Tse PW, Xu GH, et al. Analytical and numerical studies of approximate phase velocity matching based nonlinear S0 mode Lamb waves for the detection of evenly distributed microstructural changes. *Smart Mater Struct* 2016; 25(4): 045023.
34. Zuo P, Zhou Y and Fan Z. Numerical and experimental investigation of nonlinear ultrasonic Lamb waves at low frequency. *Appl Phys Lett* 2016; 109(2): 021902.
35. Shan S, Cheng L and Wen F. Characterization of non-planar second harmonic Lamb waves with a refined nonlinear parameter. *J Nondestruct Eval Diagn Progn Eng Syst* 2018; 1(1): 011004.
36. Bendsøe MP and Sigmund O. Material interpolation schemes in topology optimization. *Arch Appl Mech* 1999; 69(9): 635–654.
37. Vatanabe SL, Paulino GH and Silva ECN. Maximizing phononic band gaps in piezocomposite materials by means of topology optimization. *J Acoust Soc Am* 2014; 136(2): 494–501.
38. Holland JH. *Adaptation in natural and artificial systems*. Ann Arbor, MI: University of Michigan Press, 1975.
39. Dong HW, Su XX, Wang YS, et al. Topological optimization of two-dimensional phononic crystals based on the finite element method and genetic algorithm. *Struct Multidiscipl Optim* 2014; 50(4): 593–604.
40. Allaire G, Jouve F and Toader AM. Structural optimization using sensitivity analysis and a level-set method. *J Comput Phys* 2004; 194(1): 363–393.
41. Matsuki T, Yamada T, Izui K, et al. Topology optimization for locally resonant sonic materials. *Appl Phys Lett* 2014; 104(19): 191905.
42. Rong J, Ye W, Zhang S, et al. Frequency-coded passive multifunctional elastic metasurfaces. *Adv Funct Mater* 2020; 30(50): 2005285.
43. Liu Z, Dong HW and Yu GL. Topology optimization of periodic barriers for surface waves. *Struct Multidiscipl Optim* 2021; 63(1): 463–478.
44. Liu Y, Chillara VK and Lissenden CJ. On selection of primary modes for generation of strong internally

- resonant second harmonics in plate. *J Sound Vib* 2013; 332(19): 4517–4528.
45. Kim C. Creep damage characterization of Ni-based superalloy by acoustic nonlinearity. *Prog Nat Sci Mater Int* 2012; 22(4): 303–310.
  46. Sun X, Shui G, Zhao Y, et al. Evaluation of early stage local plastic damage induced by bending using quasi-static component of Lamb waves. *NDT&E Int* 2020; 116: 102332.
  47. Rao VVSJ, Kannan E, Prakash RV, et al. Observation of two stage dislocation dynamics from nonlinear ultrasonic response during the plastic deformation of AA7175-T7351 aluminum alloy. *Mater Sci Eng A* 2009; 512(1–2): 92–99.
  48. Ji N, Lebrun JL and Sainfort P. Broadened X-ray-diffraction profile analysis of cold-rolled aluminium-magnesium alloys. *J Mater Sci* 1994; 29(6): 1553–1557.